Numerical and Mesh Resolution Requirements for Accurate Sonic Boom Prediction of Complete Aircraft Configurations

S. Choi*, J. J. Alonso†, and E. Van der Weide‡

Department of Aeronautics & Astronautics

Stanford University, Stanford, CA 94305-3030

A careful study is conducted to assess the numerical mesh resolution requirements for the accurate computation of sonic boom ground signatures produced by complete aircraft configurations. The details of the ground signature can depend heavily on the accurate prediction of the pressure distribution in the near-field of the aircraft. It is, therefore, important to accurately describe the geometric details of complete configuration (including the wing, fuselage, nacelles, diverters, etc) and to precisely capture the propagation of shock and expansion waves at large distances from the aircraft. Unstructured, adaptive mesh technologies are are ideally suited for this purpose as they use mesh points only in the appropriate locations within the flow field. In this work, we consider a supersonic business jet (SBJ) configuration that was tested at the NASA Langley Research Center. Near-field data was measured at several locations underneath the flight track. The propagation of these near-field signatures from different altitudes can be shown to result in near N-wave ground booms. In order to examine the effect of both nacelles and empennage, results for three test cases are presented. These test cases represent the complete configuration, the configuration without the nacelles, and the configuration without the nacelles and empennage. Inviscid solution adaptive unstructured meshes with up to 7.2 million nodes and 42.1 million tetrahedra are used to calculate the pressure distributions at several locations below each configuration where comparisons with experimental data are performed. All near-field pressure distributions are propagated to the ground (from an altitude of 50,000 ft) to predict the ground boom and the perceived noise level of the ground signature. Both

*Research Associate, AIAA Member
†Associate Professor, AIAA Member
‡Research Associate, AIAA Member

the near-field overpressures and ground boom signatures are compared between experimental data and CFD simulation, and the results show good agreements in all cases. The minimum number of mesh nodes and elements and the levels of refinement needed for the accurate computations of near-field pressure distribution and ground boom signature are discussed for each of the three cases.

Nomenclature

ϵ	=	adaptation function
ϵ'	=	adaptation function with local mesh length scale
$\mathbf{V}$	=	velocity vector
∇p	=	pressure difference
$\triangle p_o$	=	initial pressure rise
$\triangle x$	=	local grid length scale
c	=	speed of sound
C_L	=	lift coefficient
L	=	aircraft body length
p	=	pressure
p_∞	=	free stream pressure
R	=	distance from the aircraft normal to the body axis
S_{ref}	=	reference area

List of Figures

List of Tables

I. INTRODUCTION

Sonic boom phenomenon is one of the main reasons preventing the acceptance of supersonic flight over populated areas. The importance of minimizing the environmental impact cannot be overstated. In addition, the business case for low-boom supersonic aircraft is also quite compelling: a much larger market can be found should the aircraft be allowed to fly supersonically over land. For these reasons research efforts have been recently focused on various techniques for sonic boom mitigation [1–7]. However, before sonic boom minimization design work can be credibly carried out, the accurate prediction of the fundamental sonic boom propagation problem has to be addressed in detail.

By the time the pressure disturbance created by an airplane reaches the ground, most boom signatures develop into the well-known N-wave shape. This signature is such that it contains two strong shocks at its beginning and end, causing a high perceived loudness (PLdB [8]). The propagation of this kind of N-wave

signatures has been pursued in the past with significant success [9–11] but without a clear understanding of the numerical requirements for the CFD portion of the problem. This has been mainly due to the lack of computational power necessary to carry out credible mesh refinement studies. These issues have important impacts on the design efforts directed towards sonic boom mitigation [6,12,13] including the techniques of the tailoring (or *shaping*) of the sonic boom signatures. Therefore, the accurate and efficient computation and propagation of N-waves and shaped booms are challenging task:to date, there have only been a few studies relating to the ability of CFD-based sonic signature methods to predict the phenomenon accurately [4,5,14].

The difficulties related to accurate analysis of sonic boom signatures with CFD methods are associated with issues of mesh resolution, artificial dissipation formulation, two-dimensional versus three-dimensional signature propagation methods, and the actual formulation of these propagation procedures. Detailed studies are needed to establish minimum requirements for the accurate analysis and design of low-boom aircraft. Those are the main purpose of the present research.

Especially regarding the mesh resolution issue, no actual guidelines have been issued yet as to the mesh element size and distribution required for accurate off-body pressure computation. This mesh resolution/distribution issue is tightly coupled with the fact that complex geometry representation (full configurations including nacelles, diverters, etc.) is typically necessary in the shaping of low sonic boom aircraft. Complete configurations also require higher mesh resolution for capturing shock and expansion waves around the aircraft.

Unstructured meshes are well suited to address the issues of automatic meshing around complete aircraft configurations and mesh resolution/distribution. They have more flexibility for adding or deleting points selectively from the computational domain. Unstructured meshes can be easily refined and coarsened adaptively with information provided by the flow solutions. This adaptive mesh refinement strategy can improve computational efficiency in the presence of finite computing resources. Depending on the resulting flow field and possible error estimates in the numerical solution, isotropic or anisotropic refinement may be more appropriate.

In this work we analyze a supersonic business jet (SBJ) configuration designed and tested at the NASA Langley Research Center that produces near N-waves at the ground plane. Basic variations of the original configuration are made by removing the nacelles and vertical tail to investigate their effects on the near field and ground boom signatures. All the analyses of aerodynamic performance and sonic boom are carried out using a tetrahedral unstructured adaptive flow solver and the PCBoom3 acoustic propagation software of Plotkin [11].

Solution adaptive meshes are generated through several adaptation and flow solution cycles. Using these meshes, near-field pressure distributions are extracted at distances of 9.5 in, 12 in and 18 in below the aircraft for each configuration (corresponding to R/L values of 0.59375, 0.75, and 1.125 respectively) and are

compared with the existing wind-tunnel data. Once the near-field data have been validated, signatures are propagated to the ground to determine the variations in signature shapes. Furthermore, noise metrics of the boom signatures are calculated for both waves propagated from experimental and computational near-field data. C-weighted sound exposure level (CSEL) and Stevens Mark VII perceived loudness level (PLdB [8]) are chosen for practical measure of sonic boom on the ground as human response to the sonic boom is more important than boom signature itself.

The objective of this work is to simply establish a minimum requirements that must be satisfied by all computations of sonic boom phenomena. For that purpose, as the results are analyzed, we suggest typical mesh and element sizes that may be required in order to produce ground boom signatures with a level of deviation less than 2 dBC and 4 PLdB respectively.

The organization of the paper is following: we describe the several components of our analysis / design tool, BOOM-UA (Unstructured Adaptive), in Section II. BOOM-UA consists of parametric CAD model generation, unstructured tetrahedral mesh generation and adaptation, flow solution and boom propagation procedure. Section III shows the three configurations of interest, wind-tunnel experiment set-ups and corresponding flow solution conditions. Results are shown at Section IV. Near-field pressure distributions from meshes with different resolutions corresponding to the various adaptation cycles are compared with wind-tunnel experimental data. Propagation of the near-field overpressure to the ground is simulated and noise metrics of boom signatures are predicted and validated using experiments and computations.

II. METHODOLOGY : BOOM-UA (Unstructured Adaptive)

BOOM-UA is a nonlinear integrated tool for both sonic boom prediction and aerodynamic performance analysis based on fully nonlinear CFD. This tool couples a three-dimensional solver for unstructured tetrahedral meshes to a CAD-based geometry kernel for efficient surface mesh regeneration, to the Centaur [15] mesh generation and adaptation system, and to the PCBoom3 software (developed by U.S. Air Force [16] and Wyle Associates [11]) for far-field signature propagation and noise metric computation. A schematic of BOOM-UA is shown at Figure 1.

The unstructured adaptive mesh generation/perturbation/regeneration capability of BOOM-UA is based on the Centaur mesh generation family of tools. Given the CAD definition of the geometry and a set of explicitly constructed far-field boundaries, Centaur uses an advancing-front method to generate both surface and volume meshes. Once a suitable mesh has been generated, the flow solution is carried out using the AirplanePlus solver of Van der Weide [17] which uses an agglomeration multigrid strategy and MPI-based parallelization to solve Reynolds-Averaged Navier-Stokes (RANS) equations on unstructured tetrahedral meshes. Although the software is able to solve the RANS equations, all calculations in this work have been

carried out using the Euler equations since the phenomena that result in ground boom signatures (shock waves and expansions) are largely of an inviscid nature, and no regions of separated flow were observed in the experiments.

We employ solution- / feature-based criteria for the mesh adaptation procedure where output functionals such as adjoint-based error estimates [18] need not be computed but only the flow variables are needed to derive the driving features of the mesh adaptation. The flow solution follows several levels of solution-based adaptation until the near-field signatures grow to be fully converged. Once such a solution is obtained, the near-field pressure signature is extracted and input to the PCBoom3 software which propagates it to the ground plane subject to a pre-specified flight altitude, atmospheric temperature profile, and horizontally stratified winds (if any, although none were used in this work). The perceived loudness (PLdB) of the ground signatures are calculated with the addition of a finite rise time and using a 1.9 ground reflection coefficient which is often used to represent an average not applicable to hard surface [6].

The whole computation from geometry description to ground boom signature and perceived noise level computation is fully automated as in Figure 1 so that optimization loops can be wrapped around the BOOM-UA system. Typical complete solution times (including all mesh generation and adaptation) are on the order of 30 minutes using 16 processors of a Beowulf cluster made up of Athlon 2100XP processors.

A. Unstructured Tetrahedral Mesh Generation

In this work we focus on the use of unstructured tetrahedral meshes for the solution of the Euler equations around complete aircraft configurations. There are numerous methods available for the generation of tetrahedral meshes [18–20] and they are typically based on either advancing front or Delaunay triangulation methods. In this work, an automatic advancing-front method is used for mesh generation. Advancing-front methods [21] involve the simultaneous generation of mesh points and their connectivity. The idea is to build the mesh element by element, adding new elements to previously generated ones, thus sweeping out a front across the entire domain. They usually rely on an explicitly defined element-size distribution function, which determines the local length scale of the element by employing a prescribed background grid and is a function of a position in the field [22]. The success of the advancing-front technique heavily relies on the existence of a this smoothly varying field function [21].

The Centaur software [15] is used in our work to construct meshes for all aircraft configurations and to enhance grid quality through automatic post processing. Only the fine meshes need to be explicitly constructed since our multigrid algorithm is based on the concept of agglomeration [23], where coarse grids are generated by fusing / agglomerating the neighboring control volumes of the fines grids, and, therefore, coarser meshes do not need to be generated directly.

The traditional approach to mesh generation using Centaur is an interactive one: a geometry import and

preparation module (*setupgrid*) is used to retrieve the surface of the aircraft configuration (usually in IGES format). This geometry representation nearly always has to be cleaned up significantly within *setupgrid* before mesh generation can proceed due to imperfections in the imported geometry definition. Once the geometry is ready for mesh generation, a surface mesh generator (*makegrid*) is used to produce the initial surface mesh on which the volume mesh will be based. Note that the IGES geometry representation is retained in the form of analytic patches so that posterior mesh adaptation is allowed to introduce nodes on the true surface of the configuration. The volume mesh is then constructed (with the same *makegrid* program) using the advancing front method. The mesh generation process includes various procedures to ensure mesh quality, including mesh smoothing.

Once a complete mesh has been created, a flow solution can be computed and the features of this flow solution can be used to add/remove nodes and elements to the mesh. This process of isotropic mesh adaptation is also carried out automatically by the Centaur module *adaptgrid*. The flow solution and mesh adaptation procedure is repeated as many times as necessary until a converged flow solution is reached, or until the memory resources of the available supercomputer were exhausted.

The process of generating a suitable mesh for sonic boom computation seems, at first, relatively user-involved. Since the requirement for user involvement can prevent the full automation of the whole BOOM-UA process (which is absolutely necessary for design) we have taken steps to ensure that no user interaction is necessary for repeated evaluation of multiple variations of a baseline configuration. This automation is not fundamental to the work presented in this paper, but is essential for design efforts that have been presented in References [24–26] for low-boom supersonic designs.

As a result, we can create parametric aircraft models [27] which can be easily regenerated when any of the shape parameters is altered. The regeneration of this CAD parametric model is driven by the CAPRI API of Haimes [28]. Once a new geometry has been constructed, the necessary information can be generated to automatically construct a volume mesh using the Centaur software modules described above and, possibly, a mesh perturbation module called *perturbgrid*. The CAPRI CAD interface also has the capability of generating surface triangulations of high quality that can be used in lieu of the ones generated internally by Centaur [29].

Figures 2 shows a typical triangular surface mesh around the NASA SBJ configuration of interest in this work. The figure contain only the triangles on the surface of the aircraft and it has been substantially coarsened for visualization purposes. Notice that the sting used for the wind-tunnel test has also been gridded.

B. Unstructured Flow Solver and Solution Approach

The three-dimensional AirplanePlus flow solver of Van der Weide [17] is used, which is a C++ implementation of the original AIRPLANE flow solver of Jameson [30]. AirplanePlus contains substantial enhancements to

the baseline algorithm, the agglomeration multigrid strategy, parallelization (of both the solver and pre-processor), load balancing algorithm, and the solution of the Reynolds-Averaged Navier-Stokes (RANS) equations.

An edge-based discretization is used to minimize the computational and memory requirements of the solver. The usual 4-stage Runge-Kutta method is modified with appropriately tailored coefficients to speed up the convergence rate by allowing high CFL numbers, aided by multigrid, residual smoothing and enthalpy damping for better convergence properties. Several options for artificial dissipation and the block-Jacobi preconditioning method are all available in the solver and can be used when needed.

An efficient, MPI-based parallelization has been shown to produce linear scalability up to 32 processors in even small meshes with around 600,000 nodes. For the type of calculations that we have carried out in this work, much larger meshes are required and, therefore, our flow solver typically scale linearly up to more than 512 processors. Typical calculations for this work have been run using 16 or 32 processors and therefore, near-linear scalability was obtained. The number of processors used was only limited by the availability of additional computational resources.

AirplanePlus has been validated on a number of configurations during its earlier use at EADS and was used to calculate accurate near-field pressure distributions for each of three SBJ configurations in this work. In addition, the flow solver from which it derives, AIRPLANE, has also undergone substantial validations studies over the years. Validation results for our SBJ configurations will be shown in Section III.C.

It must be noted that all the calculations in this work have been made using the Euler equations since they are suitable to resolve physical phenomena we are trying to predict here. However, neither the mesh generation/adaptation procedure, nor the flow solver, are limited to the Euler equations: the Reynolds-Averaged Navier-Stokes equations could also be solved at additional expense due to the increased mesh size requirements resulting from the resolution of boundary layers, shear layers, and wakes.

C. Mesh Adaptation Procedure

Once an initial solution has been computed on a tetrahedral mesh, the grid needs to be locally adapted to better capture specific features with higher accuracy at lower cost (than that obtained with either multiblock structured approaches [31] or uniform refinement of the grid.) This can be achieved through an improved distribution of grid points for each computed solution: unstructured tetrahedral elements are well suited for cell adaptation. For the cases that we have studied, coarsening has only a minor performance benefit in steady-state calculations and was omitted in this study.

The adaptation procedure utilizes h-refinement technique where the cells to be refined become parent cells and give rise to child cells by subdividing the original cells, thus grid connectivities and the number of mesh points vary correspondingly although mesh topology remains the same. Grid adaptation process is isotropic

in that we have not specified predominant directions for refinement, subdivision occurs in every direction. For each edge that is flagged for subdivision by checking if the adaptation criteria are met, new mesh nodes are inserted at the midpoint and the connectivities are redefined. For boundary edges, these points are repositioned onto the spline patch surfaces which define the original geometry from the CAD package. The current post-adaption grid-improvement scheme employs such techniques as face, and edge swapping and mesh smoothing to improve mesh quality and simulation efficiency. Undesirable shape measures (such as minimal angles) are investigated and new local tetrahedra configurations with more desirable shape measures are selected.

Figure 3(a) below shows the initial mesh around the configuration before any adaptation has taken place. Since the initial mesh resolution is critical to capture the presence of the small pressure gradients in the near-field as well as in the neighborhood of the aircraft surface, an initial mesh that is too coarse to resolve the flow features in the area close to the neighborhood of the body is avoided. In addition, the initial steps of local uniform refinement underneath the aircraft are helpful to resolve the final solution with highest accuracy. Since the presence of shock waves and expansions are the driving features to be captured and the average shock angle is relatively predictable, we initially performed two uniform local adaptations mainly in an area under the aircraft between the Mach cones of the initial and final shock waves of the fuselage of the configuration (the initial portion of the sting is also included.) Then, local mesh adaptation follows by several cycles (typically two or three) the uniform mesh adaptations in the shock regions where the pressure gradients become large. This procedure is performed recursively, and it proceeds until a certain level of error has been achieved or a maximum number of refinement levels has been accomplished.

Note that in the current study we are only interested in the effect of the primary boom carpet, and, therefore, no attempt is made to capture the shock waves that emanate from the upper surface of the configuration (which may be refracted down to the ground due to atmospheric effects.) Figure 3(b) shows the solution-adapted mesh after three adaptation steps. Typically, four or five consecutive adaptation cycles are performed automatically (starting with the initial mesh) to reach the necessary solution quality. The meshes after full adaptation cycles become too fine for display purposes, but exhibit the same features represented in Figure 3(b).

An appropriate choice of refinement criterion is very important to capture desired flow features and to obtain higher solution accuracy. The most popular refinement options for fluid-flow problems are heuristically-derived gradient-based criteria, which involve a single or multiple physical flow variables. The gradient of pressure, in general, can be used to identify inviscid flow features. But in sonic boom prediction problems the pressure gradient in the near-field is as important as in the neighborhood of the aircraft, and the direction of the gradient must be taken into account as well. A pre-specified range of velocity magnitudes which are projected onto the direction of the local pressure gradient is used for adaptation criterion. This works

successfully to predict shock locations and to capture small pressure gradients in near-field.

Our adaptation criterion is based on the local value of an adaptation function (defined as ϵ or $\epsilon^{'}$ in Equation 1 and 2 respectively) and a pre-specified area that is eligible for adaptation. If the value of the function is higher than a specified threshold value ($\epsilon = 10^{-4}$ has been used) and the edge to be adapted is within the allowable region, the mesh is subdivided for refinement. A similar approach can be used for coarsening, although it did not result in significant computational savings and was therefore not used in this study. Initially, we had focused on the following expression to represent a good indicator of the need to adapt for sonic boom computations: $\mathbf{V}$ is the velocity vector, c is local speed of sound.

$$\epsilon^{'} = \frac{\mathbf{V}}{c} \cdot \frac{\nabla p}{|\nabla p|}. \tag{1}$$

However, numerical experiments [32] by other investigators indicate that the modification of the previous equation to include a local mesh length scale $\triangle x$ such as:

$$\epsilon = \frac{\mathbf{V}}{c} \cdot \frac{\nabla p}{|\nabla p|} \triangle x \tag{2}$$

produces a more effective refinement criterion. This is partially due to the fact that while the simple gradient-based criteria decreases in magnitude as the mesh is refined in smooth regions of flow, it remains approximately constant in the vicinity of shock waves, since the shock wave profile steepens as the mesh is refined, and the jumps remain almost constant. Therefore, as the solution-based adaptation proceeds, refinement tends to occur in the area which has already been refined in the previous adaptation cycles, and near-/mid-field region away from the neighborhood of the aircraft becomes more difficult to be selected for refinement. If the restriction on the minimal length scale of the edge is considered in refinement criteria, then, even in the regions of smooth flow, the additional length scale (in the ϵ measure) can weight larger cells more heavily than small cells, and drive the adaptation process closer towards global refinement. In all of our computations, we have used the ϵ criterion which includes the pre-specified minimal allowable length scale for adaptation using Centaur's *adaptgrid*.

D. Ground Boom Propagation

The basic strategy for the computation of ground boom signatures can be seen in Figure 4 below. A solution adaptive mesh using the criteria described above is constructed around the aircraft. It extends a certain distance away from it, but not to the ground plane as it would be computationally prohibitive to do so with appropriate resolution from the cruise altitude. At the near-field plane location, the pressure signature created by the aircraft is extracted, and it is propagated down to the ground using propagation methods

based on geometric acoustics.

In this study, far-field boundaries are located about five to six body length below and above the aircraft, and the numerical results show that the far-field boundary conditions do not affect the near-field pressure distribution and extracted signals.

We have used both the PCBoom3 [11] and Sboom [33] prediction algorithms to simulate the propagation of near-field signatures to ground booms. Although the PCBoom3 software is far more capable than Sboom, we have only computed ground booms created by the aircraft in a steady-state cruise condition and, therefore, both codes showed nearly equivalent results. If ground booms caused by maneuvering aircraft were to be computed, the capabilities of the PCBoom3 software would have to be used.

There are additional extrapolation/propagation methods that are based on the concept of an Whitham's F-function [34] but these have not been used in this work as they assume axisymmetric flow with no variation of the near-field signature in the azimuthal direction, which is normally not the case in our computations.

Both PCBoom3 software and F-function based prediction method rely on results from geometric acoustics for the evolution of the wave amplitude [2], but they differ in the way to account for nonlinear waveform distortion caused by the vertical gradients of atmospheric properties and for stratified winds (which have been set to zero in this work.). Since PCBoom3 is based on Thomas waveform parameter method [2] and employs the concept of ray-tube tracing and non-linear steepening caused by the gradients in the atmosphere, it does not require such assumption of axisymmetric flow or modeling of cross-flow which are often needed for the prediction methods based on Whitham's F-function.

However, PCBoom3 still relies on the assumption of weak and isentropic wave, and near-field pressure signature should not be extracted at the location too close to the aircraft. This fact embodies one of the fundamental difficulties of the computation of accurate sonic boom signatures: the near-field must be taken sufficiently far away for the aircraft and there must be adequate mesh resolution so that the near-field signatures are accurate enough.

In this study, the pressure field at the symmetry plane 0.59, 0.75 and 1.125 body lengths below the body, is obtained and provided as an initial condition to the boom prediction software. The pressure extraction algorithm (for the unstructured tetrahedral mesh) is based on advanced octree data structures and therefore incurs very little computational cost. The overpressure signatures are extracted at a total number of 200 stations along the paths parallel to the body axis, which are properly rotated to take angle of attack effects into accounts. The effect of the number of extracting stations in the near-field on the accuracy of the propagated ground boom signals does not appear to be substantial based on the test computations which are not presented here.

It must be noted that there are more refined procedures for signature propagation [9] that allow the near-field signature to be taken closer to the aircraft (as close as 0.3 body length away), where the series of the

acoustic sources are constructed from the near-field to match the CFD solution to the far-field to be connected to ray-tracing algorithms for ground boom prediction. While more efficient in mesh resolution requirement and computation time, the method does not necessarily guarantee accurate values at small distance away, and show similar limitations on the accuracy in the near-field solutions common to the classical methods based on asymptotic F-function theory.

Depending on the type of acoustic wave propagation method used, the information extracted at the near-field can be two- or three-dimensional. In two-dimensional propagation cases (under the flight track) the pressure distribution along a line located on the aircraft symmetry plane is extracted and propagated vertically downwards. In three-dimensional wave propagation cases, the pressure data on a cylindrical surface centered along the aircraft longitudinal axis is extracted instead and propagated along rays in directions that are not necessarily perpendicular to the ground. The propagation scheme marches these *rays* down to the ground from all azimuthal directions that may eventually reach the ground. Depending on the atmospheric conditions and flight altitude, a cutoff angle will exist beyond which no disturbance will reach the ground: refraction effects divert the noise propagation back towards the upper atmosphere. Although the capability of extracting the signature on a cylinder around the aircraft is available in BOOM-UA, in this study we have chosen to extract and propagate information only under the flight track, since experimental near-field pressure data was only available on the symmetry plane.

E. Noise Metrics for Ground Boom Signature

Our earlier research on low-boom aircraft design was mainly focused on the reduction of the magnitude of only the initial peak of the ground boom signature [35]. This requirement, which had been suggested as the goal of the DARPA-sponsored Quiet Supersonic Platform (QSP) program ($\Delta p_0 < 0.3$ psf), hides the importance of the rest of the signature, which often arises from the more geometrically complex aft portion of the aircraft where empennage and engine nacelles and diverters create more complicated flow patterns. Moreover, such designs often have two shock waves very closely following each other in the front portion of the signature [14, 36], a behavior that is not robust and is therefore undesirable.

For this reason, we have chosen to make comparisons based on the noise metrics of the sonic boom signature so that more practical measure of sonic boom loudness is employed by considering human perceived noise levels. In addition to computing Stevens Mark VII perceived loudness (PLdB) [8], C-weighted sound exposure level (CSEL), is also obtained and compared with the perceived loudness. A CSEL is useful in estimating the attenuated noise when personal hearing protectors are used. Frequency weighting methods are used here due to the unique property of the human hearing system which doesn't have an equal response to sounds of different frequencies. In these calculations, less weighting is given to the frequencies to which the ear is less sensitive.

Since these types of noise metrics are calculated with full power spectra of N-wave in the frequency domain, a finite shock rise time has substantial effects on the spectra and thus on noise metric values. The ground boom signature predicted by PCBoom3 has zero shock thickness in N-wave form, which is not particularly true in reality because of non-linear variations in the atmospheric properties during propagation. PCBoom3 employs Taylor shock structure model [37] where shock thickness is modeled as hyperbolic tangent fit with an empirical thickness based on the strength of the shock. With the finite rise time added, the signal is re-interpolated/sampled at the Nyquist rate with a given bandwidth, and power spectrum of the signal is obtained by applying classical Fast Fourier Transform (FFT) to the signal (with the total number of sample points rounded up to the nearest power of two.) A single sided power spectrum by adding the powers at the frequencies with different sings is converted to the final energy spectrum by multiplying the total signal duration time. Finally weighting factor is multiplied to the signal to get weighted sound exposure level, and Stevens Mark VII method is performed to obtain perceived loudness level.

III. VALIDATION TEST CASES

A. Supersonic Business Jet Configuration

A supersonic business jet (SBJ) configuration we are simulating was tested in the Unitary Plan Wind Tunnel (UPWT) in NASA Langley Research Center, and was used to extract near-field pressure information at various distances from the aircraft model. Variations of the baseline configuration are created by the removal of the nacelles and vertical tail in order to investigate their effect on both the near-field pressure distributions and the ground boom signature.

The original configuration was developed by Mack [38, 39] and was tested by Wilcox and Coen [40]. It consists of a wing with large outboard dihedral/winglet, fuselage, vertical tail, and aft-fuselage mounted nacelles with diverters attached to the fuselage. The top, front, side and perspective views of the configuration as analyzed (including the rear sting mount) can be seen in Figure 5. Details of the experimental model and the testing procedure can be found in reference [40].

For purposes of computing the ground boom signatures, the wind-tunnel models were scaled up by a factor of 100 (as suggested by the wind-tunnel test report) and were flown at a cruising altitude of 50,000 ft on a U.S. Standard Atmosphere with no winds [41]. For a target lift coefficient $C_L = 0.1$ based on a scaled reference area of $S_{ref} = 1560\ ft^2$ these conditions result in an aircraft cruise weight of 105,790 lbs. The model length is 16 inches without the sting and 42 inches with the sting included. The case with nacelles included uses what are referred to as *big nacelles* in the wind-tunnel report.

BOOM-UA is applied to all three configurations to extract the near-field overpressures and to predict accurate ground boom signatures: AirplanePlus in BOOM-UA is used for flow solution, and near-field

overpressure extraction. PCBoom3 is used for ground boom prediction. The near-field overpressures are extracted at three distances from the aircraft model (9.5 inches, 12 inches, and 18 inches) corresponding to the locations where experimental data were taken. This allows us to compare the CFD predictions directly with experiment and to compute ground signatures propagated from these distances. If all three pressure signatures were sufficiently far from the aircraft the computed ground boom signatures would fall on top of each other. As will be shown in Section IV, this is not the case, although the differences in both the ground boom signatures and the perceived loudness are relatively small.

B. Experimental Setup

The wind tunnel test was conducted in the NASA Langley Unitary Plan Wind Tunnel (UPWT) which is a continuous flow, variable pressure supersonic wind tunnel. The tunnel contains two test sections which are approximately 4 ft^2 and 7 ft long. The Mach number for the relevant experiments was set 2.0, while Reynolds number based on the chord length was 2.0×10^6 per ft.

The model and sting combination were pinned together and connected to an angle of attack mechanism and tunnel model support system. The angle of attack mechanism was used to vary the model angle of attack. The tunnel model support system had the capability to move the model longitudinally and laterally within the test section so that near-field pressure signatures could be extracted at varying distances from the model. A lift balance was installed in the test model and used to measure the lift coefficients. The survey and reference probes were mounted on a track to measure the difference between the static pressure of each probe. The near-field pressure was measured at three different locations for each configuration with different angles of attack. Although the existence of the sting in the test model may change the aft portion of the flow field below the model, disturbance affects the regions behind the shock coming from tail and nacelles, where we do not extract much overpressure data. Experimental data measured by survey probe appear to truncate those portions in the near-field data A CAD model and corresponding computation mesh for CFD simulation includes the sting, however the mesh adaptation is not performed below the sting region to exclude the effects of sting on the near-field pressure.

Figure 6 is reproduced from the experimental report [40] and shows a brief view of the experimental model mounted in the wind tunnel.

C. Flow Conditions

BOOM-UA was used to simulate the results from the wind-tunnel experiments, and the flow solver portion of BOOM-UA (AirplanePlus) was used in inviscid mode only. In all of these computations, small discrepancies may therefore exist due to the lack of viscous effects, although these discrepancies are expected to be small, as viscosity only plays a minor role in the generation of the pressure signatures that we are interested in.

In addition, the angle of attack was set to match the experimental values for each of configurations and varies from 2.54° to 2.89°. It should be noted that no attempt was made to match the experimental lift coefficients exactly and variations in angle of attack, static pressure and other properties are not taken into account in CFD simulation. As expected, the computed lift coefficients (at the matched angles of attack) are approximately 1% higher than the experimental values obtained, however, the lift coefficients are very close to $C_L = 0.1$ in all cases. The cruising altitude is set at 50,000 ft.

Figures 7, 8 and 9 show the surface pressure distributions obtained by the AirplanePlus flow solver on each of the three configurations of interest. Notice that each successive set of figures presents the configuration with components (nacelles and empennage) removed. No specific boundary conditions for the nacelles have been specified, as the changes in mass flow through the nacelles were not available. The flow in CFD simulation is modeled to pass through the nacelle with free stream velocity. Note that wind-tunnel test did not use screens in nacelles. It is expected that inlet-lip shocks from the nacelles can have signifiant effects on the near-field pressure (compare Figure 10 and 11). The effects of the existence of the nacelles are also shown in CFD simulation, and the capability of the flow solutions to capture the details of the shock structure caused by the presence of the nacelles and diverters in the aft portion of the geometry is shown in Figure 7, 8, and 9 .

It should also be noted that the uncertainties in CFD simulation, wind-tunnel experiment, and boom propagation procedure must be taken into accounts. As our simulation is carried out using Euler computation, the viscous effects are excluded while assuming those impacts are not dominant. The effect of numerical dissipation in CFD algorithm can also affect the near-field solutions. Imposition of proper physical boundary condition for nacelle and matching the lift coefficients rather than angle of attacks need to be considered. For wind-tunnel experiment, static pressure is not exactly matched with free stream pressure. To obtain ground boom signature, the models are scaled up to a real size, and near-field signatures from computations and experiments in model size are propagated to a real ground signature to calculate the realistic noise metrics. There may be uncertainties in scaling in near-field pressure and ground boom signatures.

IV. RESULTS

A. Pressure Distributions vs. Mesh Resolution

In order to assess the mesh resolution requirements for accurate near-field signature extraction, solution-adaptive computations were carried out for each of the three configurations in question (c1 = full configuration, c2 = configuration without nacelles, c3 = configuration without nacelles and tail). For each of these configurations, five flow solutions and four adaptation cycles were carried out starting from relatively fine initial meshes.

Table 1 shows the number of nodes in each mesh, for each adaptation cycle, and for each configuration (c1 through c3.) The resolution of the initial mesh is important to ultimately calculate all of the phenomena we intend to capture. This is particularly true of the small pressure gradients in the near field (compared to those in a close neighborhood of the body) which tend to be missed if the initial mesh resolution is not sufficiently fine (the adaptation criterion explained at Section II.C focuses on the flow features near the aircraft and disregards the near-field flow features.) For this reason, all initial meshes contained between 500,000 and 600,000 nodes. The first two levels of adaptation are uniform isotropic refinement in the area between the expected location of the front and rear shocks of the configuration. The third and fourth adaptation cycles are performed on solution-based criteria.

After four adaptation cycles, the near-field pressure distributions appear to have converged. In the case of the configuration without nacelles and tail (c3) a further attempt to an additional adaptation level failed due to *adaptgrid* exceeding the memory requirements of our Origin300 computer (16 Gbytes maximum). Note that all of the final meshes, whose solutions will be used for experimental comparison, have between 7×10^6 and 8×10^6 nodes. We can infer that this large number of nodes is necessary to obtain reasonable comparisons that capture all of the flow features of the experiment. This mesh size (on an adaptive mesh) is in contrast with our earlier work [31] (using multiblock structured meshes which had been biased along the direction of the front and rear shocks) which used on the order of 3×10^6 nodes.

The differences in pressure distribution on the surface and in the near-field for all three configurations are clearly seen in Figures 7 through 9, and Figure 13 respectively. The front portion of the signatures are almost identical as the geometries in that area are same and the removal of the tail and nacelle do not affect the pressure distributions upstream. However, the rear portion of the signature shows differences. The omission of the nacelles results in a sharp decrease in strength of second to last shock in the distribution. This can be appreciated from Figures 7 and 8 where the complex system of shock waves in the aft portion of the fuselage has disappeared. The effect of the removal of the tail (see Figure 9) is not as dramatic, but does cause an alteration in the pressure signature: the strength of the last shock wave in the signature is reduced to a $\Delta p/p < -0.02$.

Figures 14 through 16 show the evolution of the near-field pressure distributions through the various adaptation cycles for all three configurations. For each configuration, we present computational results for each of the three near-field distances at which (at least for the complete configuration) data was taken in the wind tunnel. The locations at which computational data was extracted are lines on the symmetry plane located at distances of r = 9.5 inches, r = 12 inches, and r = 18 inches under the aircraft. As expected, the finest mesh for each configuration resolves the pressure signatures with most detail: the pressure rise across the shock is largest at each location and some of the minor features of the signature are present, while the coarser meshes do not capture those.

It can also be noted that the overpressure distributions that result from the mesh after three adaptation cycles (with around 3×10^6 nodes do not necessarily capture all the details of the signature and certainly miss the peak values of all of the shocks in the signature. From these observations we conclude that around 10×10^6 nodes are necessary to ensure that the near-field pressure signatures are computed without numerical error. However, the most important aspect to a designer is not the level of error in the near-field pressure signature, but the resulting errors once the near-field signature has been propagated to the ground. As we will see in a later section, due to the process of shock coalescence (as the signature ages) if the ground boom has an N-wave character, the need for the absolutely highest resolution in the near field may not be justified. However, for cases where the signature is such that it is *shaped*, the resolution we have discussed here is needed.

B. Comparison of Near-field Pressures with Experimental Data

From the results of the mesh resolution study, the solution from the finest mesh (after four or five solution adaptive refinements) was chosen for comparison with the near-field pressures obtained from the wind-tunnel test. These comparisons are presented in Figures 10 to 12. For the cases without nacelles and tail, experimental data was not collected at the r = 12 inch location and, therefore, a direct comparison is not available. It should also be noted that since the reference pressure during the experimental runs was not necessarily p_∞, the signatures do not start and end at values of $\Delta p/p = 0$. For this reason, the experimental signatures have been shifted (no scaling applied) in such a way that $\Delta p/p = 0$ was obtained at the front and rear of the signatures.

In general, good agreement between the experiment and computations is found, despite the fact that all computations were carried out using the Euler equations and viscous effects were neglected. Furthermore, all computations were carried out at the experimentally determined angle of attack (no attempt to match C_L was made.) In addition, the computations simulated the aircraft embedded in a free stream and did not enclose the model within the wind-tunnel walls.

The number and magnitude of all pressure peaks in the experimental near-field signatures are captured by the simulations for all three configurations. Some small details in the aft portion of the signatures, particularly for the configuration without nacelles and without tail in Figure 11 and 12, are missing from the computations. This fact denotes that initially finer mesh in the back end of the aircraft may be necessary for the adaptation procedure to capture these features. However, these features have small magnitude and are absorbed by the aging of the signature as it propagates down to the ground.

There is a slight tendency to overpredict the absolute length of the signature (from initial to final shock) in comparison with the experiment, which indicates that either the angles of the leading and trailing shocks were not predicted exactly, or that the effect of the expansions on the shock angles in the near field were

slightly off. Again, these slight discrepancies do not appear to translate into significant ground perceived loudness changes, which are shown at Section IV.C.

Some of these effects can be seen in the symmetry-plane pressure plots shown for all three configurations in Figure 13. The effects of both the nacelles and tail on the near-field pressure can be seen by comparing the three symmetry-plane pressure plots. The shocks that emanate from the tail region in the cases without nacelles and/or tail weaken considerably in comparison with the wave pattern present for the full configuration.

C. Ground Boom Signature and Weighted Sound Exposure Levels

Finally, in this section we present the results of the propagation of both computed and experimentally-determined near-field signatures to the ground with the wind-tunnel model scaled up by a factor of 100 for the full-scale aircraft. In addition, the cruise altitude for the full-scale aircraft was chosen to be 50,000 ft, and a Standard US Atmosphere with no winds [41] was setup for propagation purposes. The cutoff angle for acoustic disturbances that reach the ground turns out to be $\pm 54^{\circ}$, although only signatures underneath the flight track are considered here. All ground boom signatures are computed using the PCBoom3 software.

The ground boom signatures obtained starting from both experimental and computational near-field pressure distributions are presented in Figures 17, 18 and 19. The plots in Figures show the results only after one and five adaptation cycles, and this is to highlight the differences that derive from the use of much smaller meshes. We can see from Figures that the ground signatures for these configurations result in pressure distributions that are very similar to an N-Wave, except for the fact that a small shock persists in the middle of the signature (that has not yet been absorbed by either the front or rear shocks.) The computationally determined signatures exhibit an additional shock (in the front of the signature) that is not present in the ground booms propagated from near-field overpressure from the experiments: it appears that the small differences in the computational and experimental near-field pressure (after the initial pressure rise) are such that they are delaying the final coalescence of the front two shocks (when compared to the experimental results). Additional propagations of the same computational signatures from higher altitude (55,000 ft for example) show a fully coalesced front shock.

The differences in character between the computational and experimental ground boom signatures are not very large. In the case where the ground signature is nearly an N-wave, even the coarser meshes result in ground signatures that agrees well with those propagated from experimental data. The most distinctive tendency, however, is that as the number of mesh adaptation levels increases, the peak overpressures in the ground signatures increase, sometimes by up to 20%. These peak overpressures are consistently 5-7% lower than the experiment. Therefore, in order to predict the actual values of the peak overpressures, it is necessary to use the finest meshes in the adoption sequence, if not even slightly finer ones.

A more quantitative measure of the differences in the ground booms is presented below. Both C-weighted sound exposure level (a measure that is useful to determine human perceived noise when wearing protective equipment) and perceived loudness were calculated for both computations and experiment. Tables 2, 3 and 4 show the two sound level representations for the boom signature derived from the experimental data and CFD simulation. Each table corresponds to each of the different configurations. The deviations of the two sound level representations between ground signatures obtained from the finest meshes and from experimental data are shown in Tables. For all three configurations and at all three different near-field locations, the sound levels of the propagated ground boom produce only small deviations. In fact, the average deviation is around 2 dBC for the C-weighted sound exposure level, and slightly larger (around 4.17 PLdB) for the perceived loudness level.

V. CONCLUSIONS

We have developed a tool for sonic boom analysis of complete aircraft configurations, BOOM-UA, which automates the complete process from parametric CAD definition to ground boom loudness measures. The methodology is based on a direct CAD interface (CAPRI), the Centaur mesh generation and adaptation procedure, the unstructured tetrahedral flow solver AirplanePlus, and the PCBoom3 signature propagation program. Although the focus of this paper was on the validation of our tool using wind-tunnel data, BOOM-UA is intended in design environment.

A set of unstructured adaptive solutions were calculated for three configurations of interest (obtained by removing the nacelles and tail from a baseline configuration) and near-field pressure distributions were extracted, for each case, at three distances underneath the aircraft on the symmetry plane. These near-field pressure distributions are compared with the experimental values and are found to be in very good agreement for meshes with over 7×10^6 nodes.

The computed near-field pressure signatures were propagated to the ground from an altitude of 50,000 ft and the resulting signatures were compared with those obtained using the experimental near-field data. Deviations in both perceived loudness and C-weighted sound exposure level are found to be within 2 dBC and 4 PLdB from the experimentally derived values.

Based on this study, the following key conclusions are drawn: 1) the use of unstructured solution-adaptive mesh enables our study to provide a reasonable guidance on the numerical requirements on CFD simulation to accurately predict the sonic boom. 2) the automated analysis tool in combination with a practical choice of noise metrics for sonic boom prediction has great potential for design optimization of low-boom supersonic business jets.

VI. ACKNOWLEDGMENTS

This work has been carried out under the support of the NASA Langley Research Center, under contract NAG-1-03046. We gratefully acknowledge the support of our point of contact, Dr. Peter Coen, in supplying us with the geometry and experimental data necessary to complete this study.

References

[1] Plotkin, K. J., "Review of Sonic Boom Theory," AIAA Paper 89-1105, Apr. 1989.

[2] Thomas, C., "Extrapolation of Sonic Boom Pressure Signatures by the Waveform Parameter Method," NASA TN D-6832, 1972.

[3] Whitham, G. B., "The Flow Pattern of a Supersonic Projectile," *Communications on Pure and Applied Mathematics*, Vol. 3, 1952, pp. 301–348.

[4] Cheung, S. H., and Edwards, T. A., "Supersonic Airplane Design Optimization Method for Aerodynamic Performance and Low Sonic Boom," *In High-Speed Research Conference: Sonic Boom,* Volume II, NASA Ames Research Center, Feb. 1992, pp. 31–44.

[5] Siclari, M. J., "Ground Signature Extrapolation of Three-Dimensional Near-Field CFD Predictions for Several HSCT Configurations," *In High-Speed Research Conference: Sonic Boom,* Volume II, NASA Ames Research Center, Feb. 1992, pp. 175–200.

[6] Seebass, R., and Argrow, B., "Sonic Boom Minimization Revisited," AIAA Paper 98-295, Jun. 1998.

[7] Nadarajah, S., Jameson, A., and Alonso, J. J., "An Adjoint Method for the Calculation of Remote Sensitivities in Supersonic Flow," AIAA Paper 2002-0261, Jan. 2002.

[8] Stevens, S. S., "Perceived Level of Noise by Mark VII and Decibels (E)," *Journal of the Acoustical Society of America,* Vol. 51, No. 2, 1972, pp. 575–60.

[9] Page, J., and Plotkin, K., "Extrapolation of Sonic Boom Signatures from CFD Solutions," AIAA Paper 2002-0922, Jan. 2002.

[10] Cliff, S. E., and Thomas, S. D., "Euler/Experiment Correlations of Sonic Boom Pressure Signatures," AIAA Paper 91-3276, Sep. 1991.

[11] Plotkin, K. J., "PCBoom3 Sonic Boom Prediction Model-Version 1.0e," Wyle Research Report, WR 95-22E, Oct. 1998.

[12] Howe, D. C., "Improved Sonic Boom Minimization with Extendable Nose Spike," AIAA Paper 2005-1014, Jan 2005.

[13] Pawlowski, J. W., Graham, D. H., Boccadoro, C. H., Coen, P. G., and Maglieri, D. J., "Origins and Overview of the Shaped Sonic Boom Demonstration Program," AIAA Paper 2005-5, Jan. 2005.

[14] Chan, M., "Supersonic Aircraft Optimization for Minimizing Drag and Sonic Boom," PhD thesis, Stanford University, Stanford, CA 94305, 2003.

[15] "Centaur Users' Guide", http://www.centaursoft.com/support/manual.

[16] Plotkin, K. J., Downing, M., and Page, J. A., "USAF Single-Event Sonic Boom Prediction Model: PCBoom3," *High-Speed Research 1994 Sonic Boom Workshop Atmospheric Propagation and Acceptability Studies*, NASA Langley Research Center, Vol. 14, pp. 171-184, Oct. 1994.

[17] Fornasier, L., Rieger, H., Tremel, U., and Van der Weide, E., "Time Dependent Aeroelastic Simulation of Rapid Maneuvering Aircraft," AIAA Paper 2002-0949, Jan. 2002.

[18] Park, M. A., "Adjoint-Based, Three-Dimensional Error Prediction and Grid Adaptation," AIAA Paper 2002-3286, Jun. 2002.

[19] Lohner, R., "Generation of Unstructured Grids Suitable for RANS Calculations," AIAA Paper 99-0662, 1999.

[20] Baker, T. J., "Mesh Adaptation Strategies for Problems in Fluid Dynamics," *Finite Elements in Analysis and Design*, Vol. 25, 1997, pp. 243-273.

[21] Mavriplis, D. J., "Unstructured Mesh Generation and Adaptivity," *ICASE* 95-26.

[22] Peraire, J., Mahdati, M., Morgan, K., and Zienkienwicz, O. C., "Adaptive Remeshing for Compressible Flow Computation," *Journal of Computational physics,* Vol. 72, 1987, pp. 449–466.

[23] Mavriplis, D. J., and Jameson, A., "Multigrid Solution of the Two-Dimensional Euler Equations on Unstructured Triangular Meshes," *AIAA Journal,* Vol. 30, No. 7, 1992, pp. 1753–1761.

[24] Choi, S., Alonso, J. J., and Chung, H. S., "Design of a Low-Boom Supersonic Business Jet Using Evolutionary Algorithms and an Adaptive Unstructured Mesh Method," AIAA Paper 2004-1758, Apr. 2004.

[25] Choi, S., Alonso, J. J., Kroo, I. M., and Wintzer, M., "Multi-fidelity Design Optimization of Low-boom Supersonic Business Jets," *Journal of Aircraft,* Vol. 45, No. 1, 2008, pp.106–118.

[26] Choi, S, Alonso, J. J., Kroo, I., and Wintzer, M., "Two-Level Multi-Fidelity Design Optimization Studies for Supersonic Jets" AIAA Paper 2005-0531, Jan. 2005. NV.

[27] Alonso, J. J., Martins, J. R. R. A., Reuther, J. J., Haimes, R., and Crawford, C. A., "High-Fidelity Aero-Structural Design Using a Parametric CAD-Based Model," AIAA Paper 2003-3429, Jun. 2003.

[28] Haimes, R., "CAPRI: Computational Analysis Programming Interface," *Proceedings of the 6th International Conference on Numerical Grid Generation in Computational Field Simulations*, Jul. 1998.

[29] Haimes, R., "Automatic Generation of CFD-Ready Surface Triangulations from CAD Geometry," AIAA Paper 99-0776, 1999

[30] Jameson, A., Baker, T. J., and Weatherill, N. P., "Calculation of Inviscid Transonic Flow Over a Complete Aircraft," AIAA Paper 86-0103, Jan. 1986.

[31] Chung, H. S., Choi, S., and Alonso, J. J., "Supersonic Business Jet Design Using a Knowledge-Based Genetic Algorithm with an Unstructured, Adaptive Grid Methodology," AIAA Paper 2003-3791, Jun. 2003.

[32] Warren, G., Anderson, W. K., Thomas, J. L., and Krist, S. L., "Grid Convergence for Adaptive Methods," AIAA paper 91-1592, Jun. 1991.

[33] Thomas, C. L., "Extrapolation of Wind-Tunnel Sonic Boom Signatures without Use of a Whitham F-function," NASA SP-255, 1970, pp.205–217.

[34] Hayes, W. D., Haefeli, R. C., and Kulsrud, H. E., "Sonic Boom Propagation in a Stratified Atmosphere, with Computer Program," NASA CR-1299, 1969.

[35] Alonso, J. J., Kroo, I. M., and Jameson, A., "Advanced Algorithms for Design and Optimization of Quiet Supersonic Platforms," AIAA Paper 2002-0114, Jan. 2002.

[36] Chung, H. S., "Multidisciplinary Design Optimization of Supersonic Business Jets Using Approximation Model-Based Genetic Algorithms," PhD thesis, Stanford University, Stanford, CA 94305, 2004.

[37] Taylor, G. I., "The Conditions Necessary for Discontinuous Motion in Gases" *Proceedings of the Royal Society, London*, A84, 1910, pp. 371–377.

[38] Mack, R. J., "A Supersonic Business-Jet Concept Designed for Low Sonic Boom," NASA/TM-2003-212435, NASA Langley Research Center, Oct. 2003.

[39] Mack, R. J., "An Analysis of Measured Sonic-Boom Pressure Signatures From a Langley Wind-Tunnel Model of a Supersonic-Cruise Business Jet Concept, " NASA/TM-2003-212447, NASA Langley Research Center, Oct. 2003.

[40] Wilcox, F. J., "Business Jet Sonic Boom Test - Unitary Plan Wind Tunnel Test 1870," NASA Langley Research Center, Feb. 2000.

[41] U.S. Standard Atmosphere, U.S. Government Printing Office, Washington, D. C., 1962.

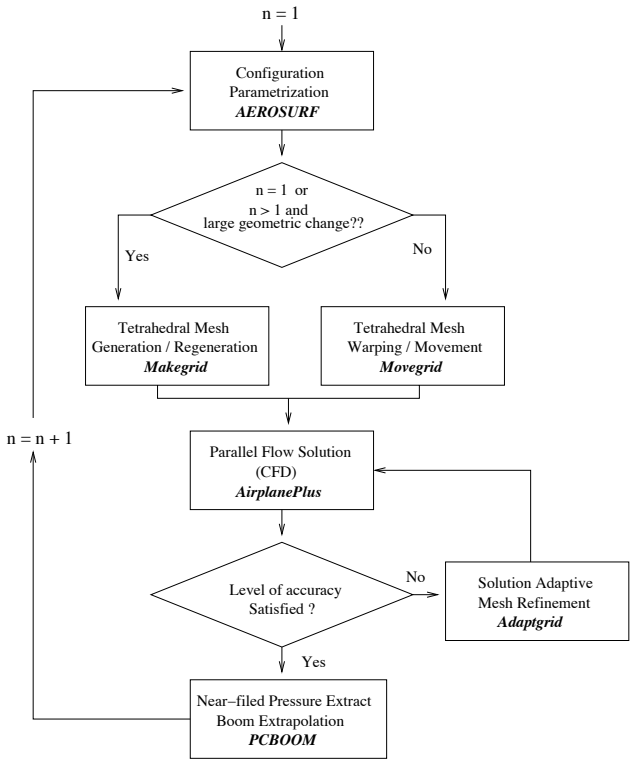

Figure 1. Schematic of the aerodynamic analysis tool, BOOM-UA

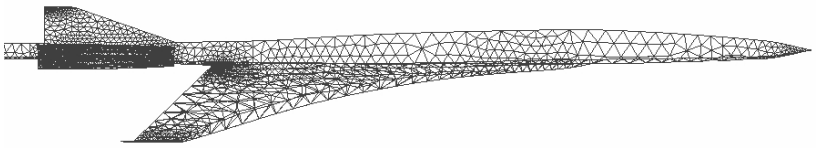

Figure 2. Surface mesh for NASA SBJ configuration.

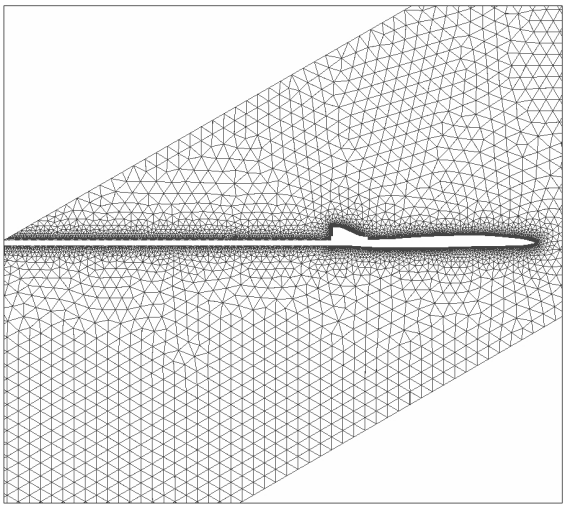

(a) Original mesh without adaptation, Mesh nodes=607,787

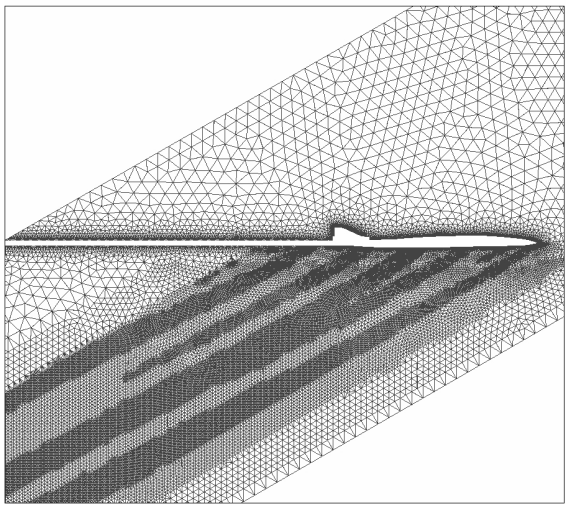

(b) Mesh after three adaptations with mesh nodes=1,893,110

Figure 3. Mesh apaption procedure

	Initial	1^{st} adpt	2^{nd}adpt	3^{rd}adpt	4^{th} adpt
c1	607,787	690,239	933,192	2,749,606	7,698,731
c2	543,201	591,056	854,781	2,737,821	7,973,972
c3	523,954	572,467	838,612	2,736,989	8,100,624

Table 1. Number of mesh nodes through all the adaptation cycles

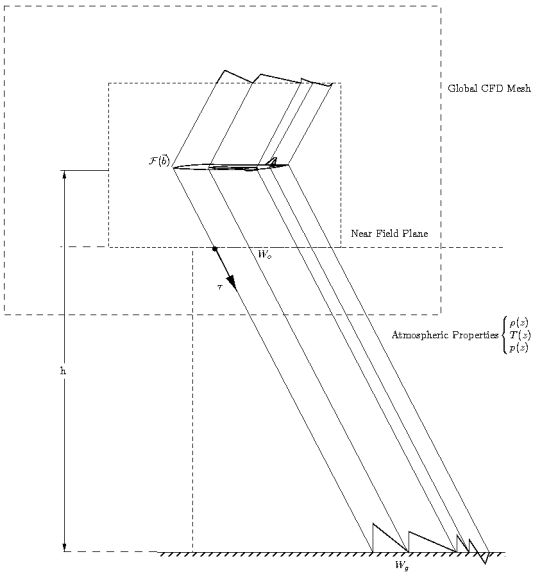

Figure 4. Schematic of Sonic Boom Minimization Setup with Nomenclature.

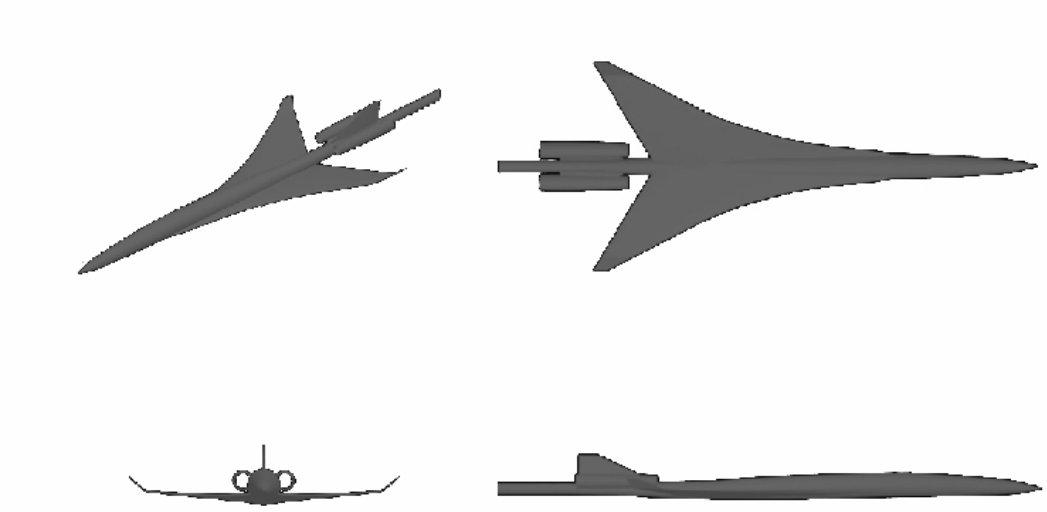

Figure 5. Three-View drawing of NASA SBJ configuration.

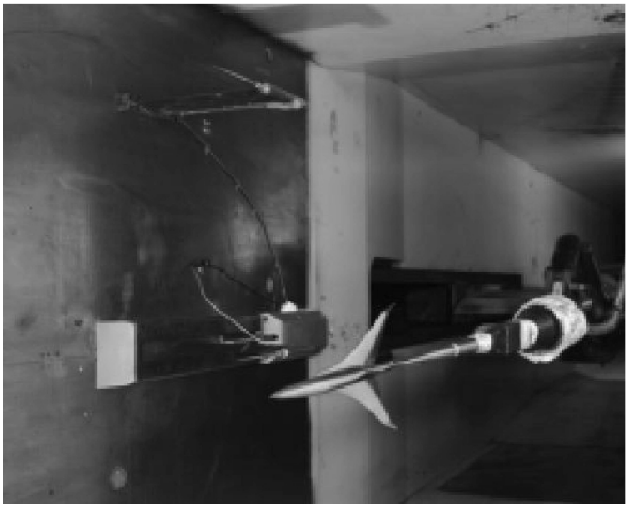

Figure 6. View of the model mounted in the wind tunnel.

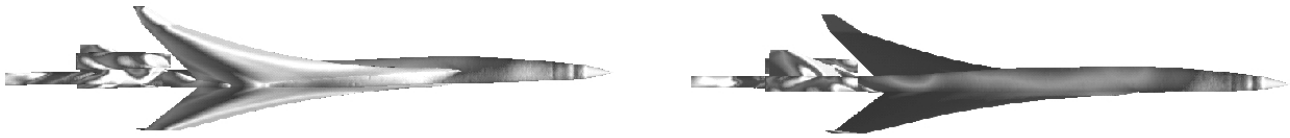

(a) Lower surface. (b) Upper surface.

Figure 7. Surface pressure distributions: complete configuration SBJ (low pressure: black, high pressure: white.)

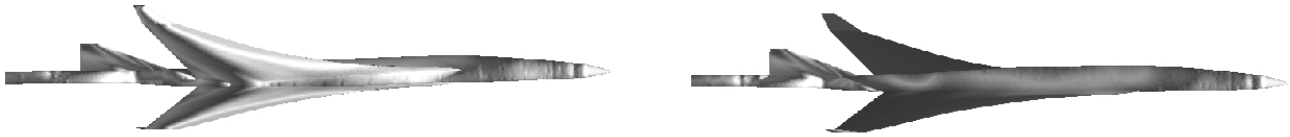

(a) Lower surface. (b) Upper surface.

Figure 8. Surface pressure distributions: SBJ without nacelles (low pressure: black, high pressure: white.)

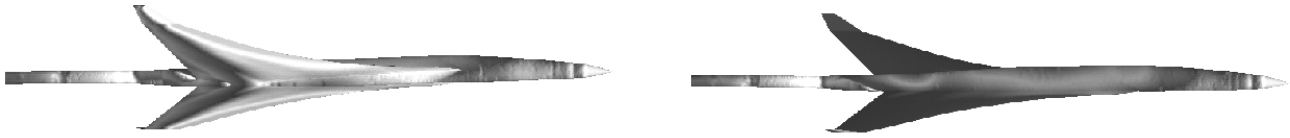

(a) Lower surface. (b) Upper surface.

Figure 9. Surface pressure distributions: SBJ without nacelles and empennage (low pressure: black, high pressure: white.)

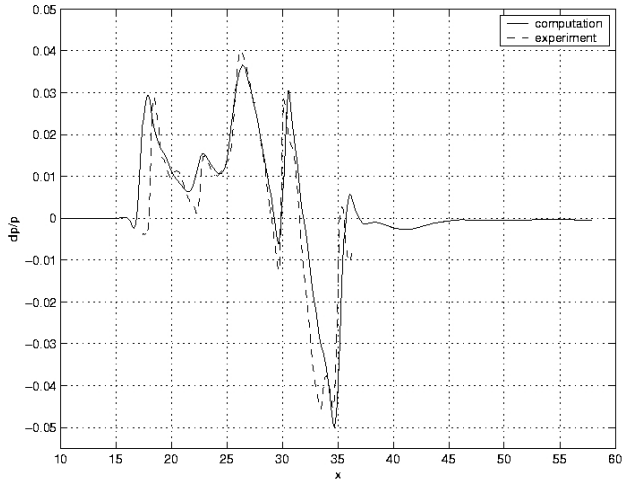

(a) Pressure distribution at r=9.5 in

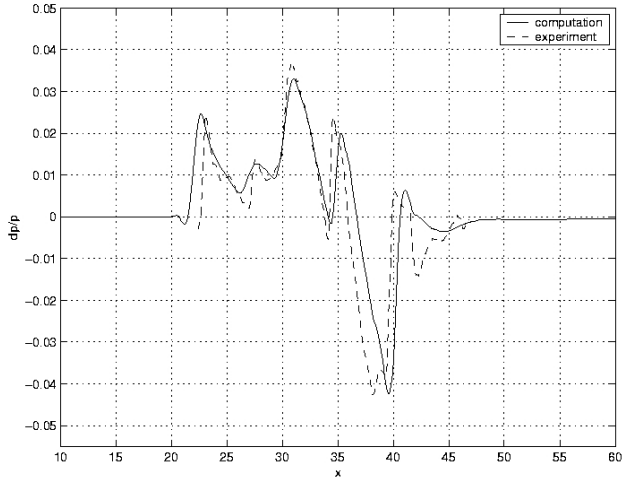

(b) Pressure distribution at r=12 in

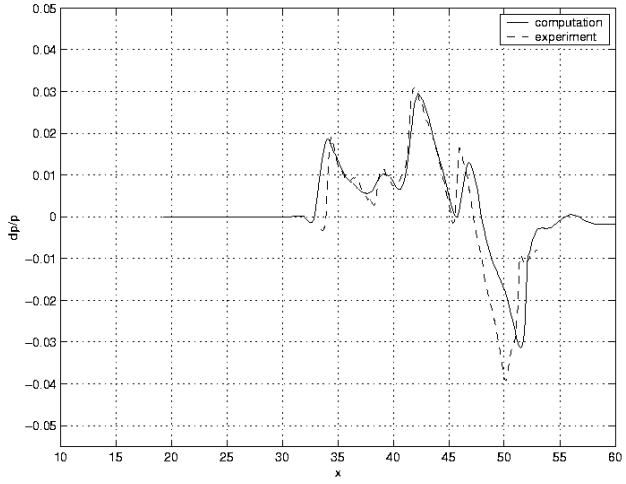

(c) Pressure distribution at r=18 in

Figure 10. Comparison of near-field pressure with experiments. Complete configuration.

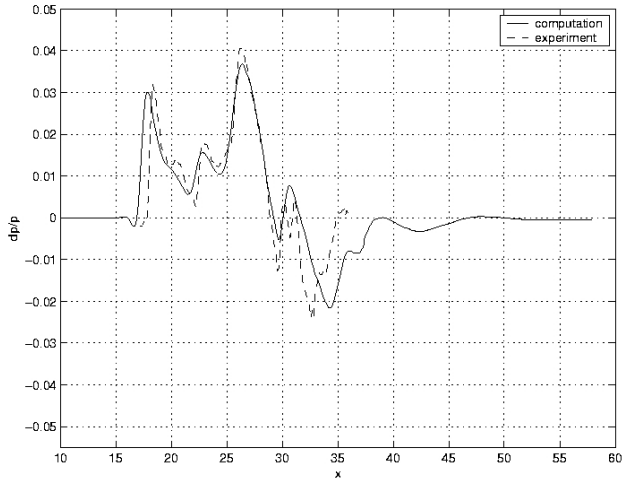

(a) Pressure distribution at r=9.5 in

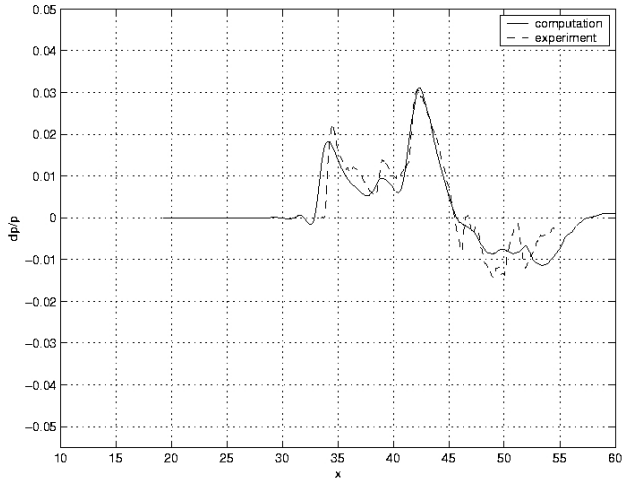

(b) Pressure distribution at r=18 in

Figure 11. Comparison of near-field pressure with experiments. Configuration without nacelles.

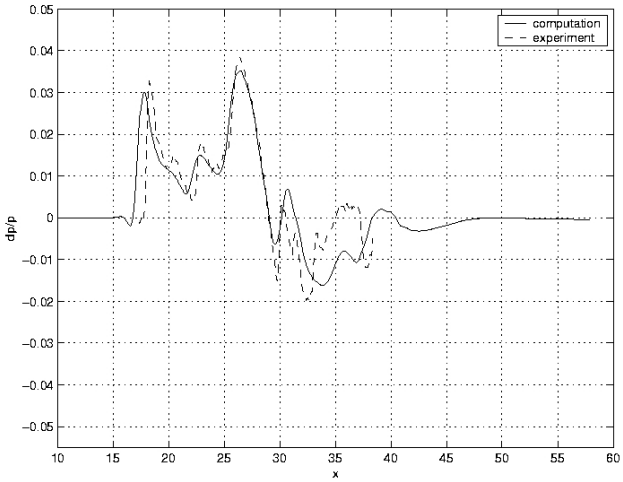

(a) Pressure distribution at r=9.5 in

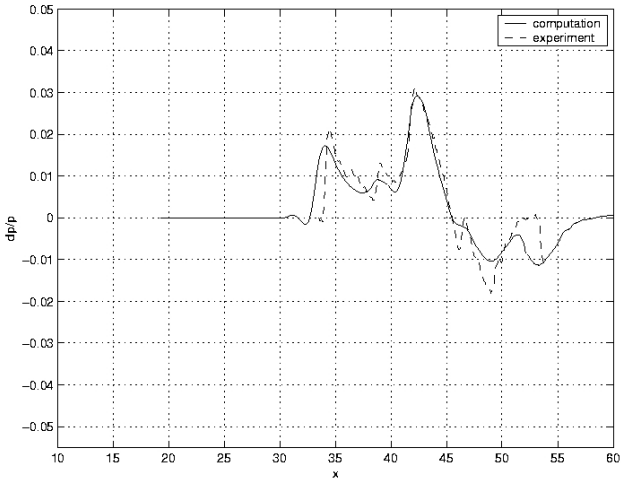

(b) Pressure distribution at r=12 in

Figure 12. Comparison of near-field pressure with experiments. Configuration without nacelles and tail.

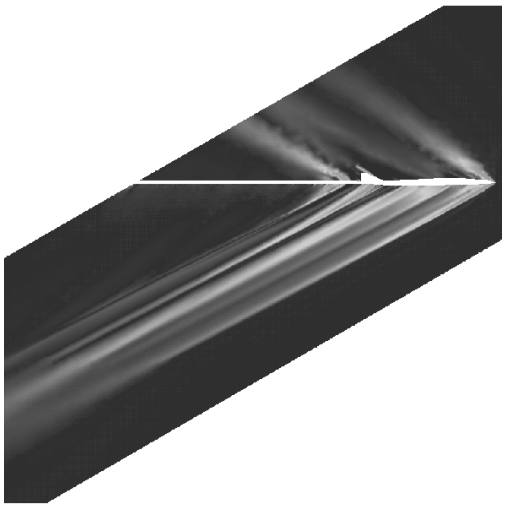

(a)Pressure distribution for complete configuration.

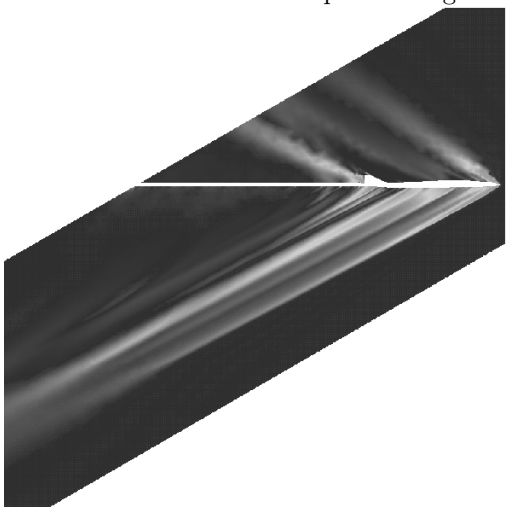

(b)Pressure distribution for configuration without nacelles.

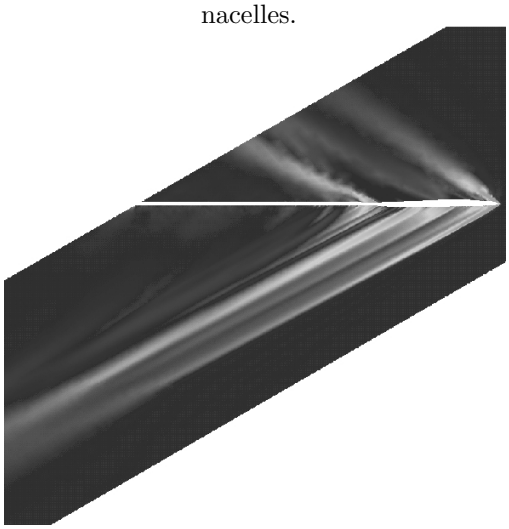

(c)Pressure distribution for configuration without nacelles and tail.

Figure 13. Plot of near-field pressure distributions along symmetry plane (low pressure: black, high pressure: white.)

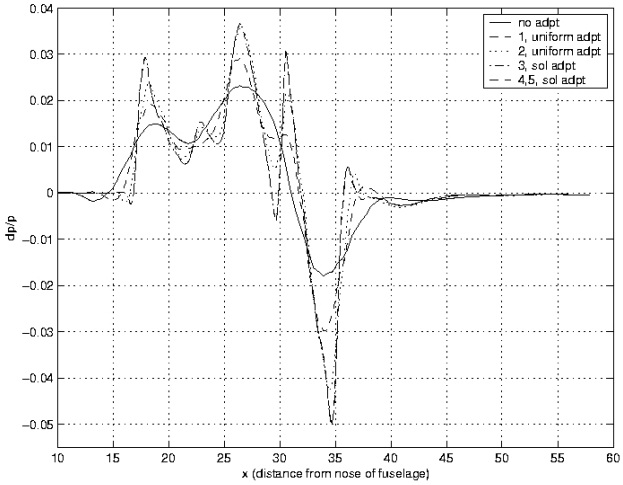

(a) Pressure distribution at r=9.5 in

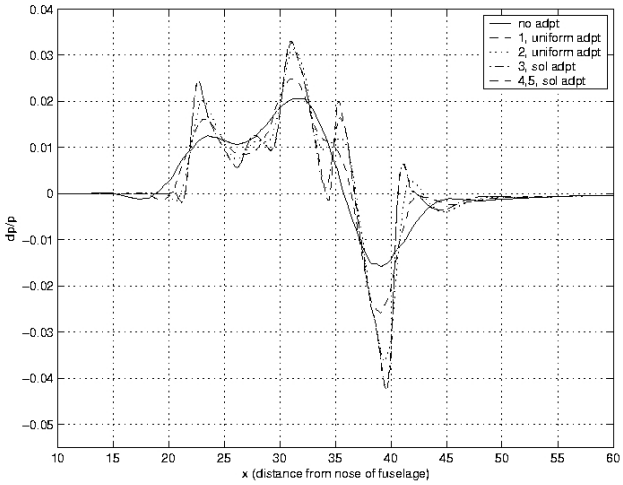

(b) Pressure distribution at r=12 in

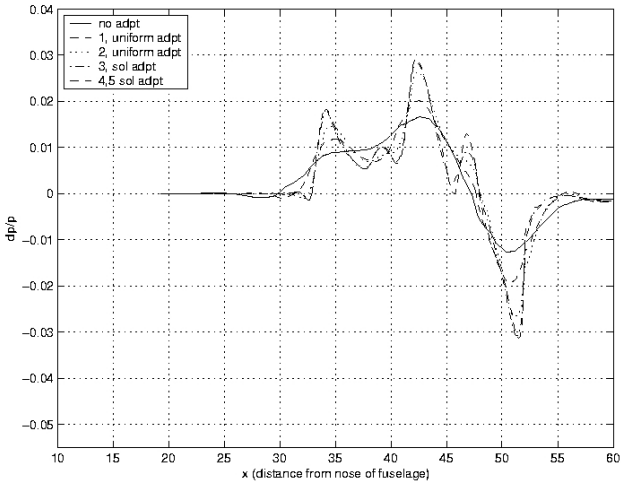

(c) Pressure distribution at r=18 in

Figure 14. Near-field pressure distributions for all adaptation cycles. Complete configuration.

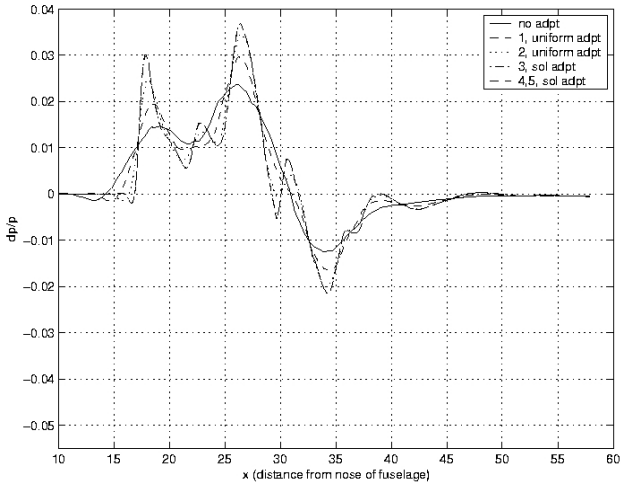

(a) Pressure distribution at r=9.5 in

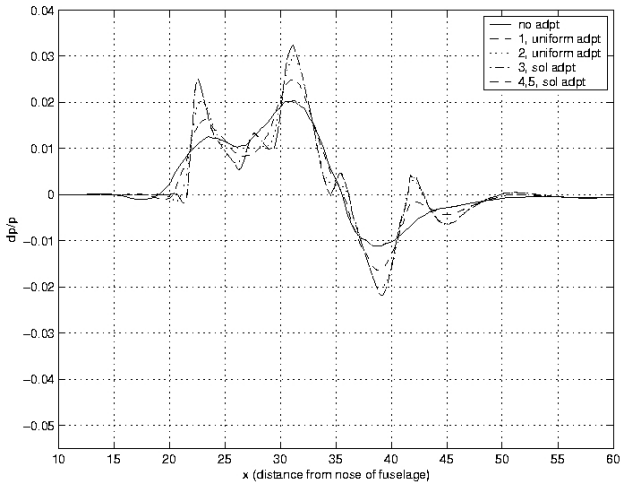

(b) Pressure distribution at r=12 in

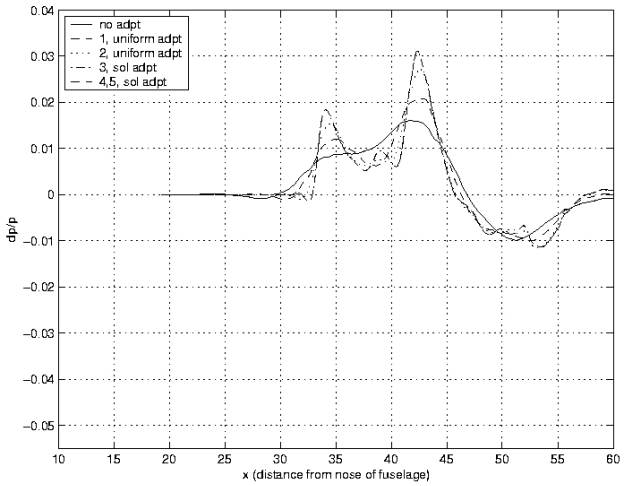

(c) Pressure distribution at r=18 in

Figure 15. Near-field pressure distributions for all adaptation cycles. Configuration without nacelles.

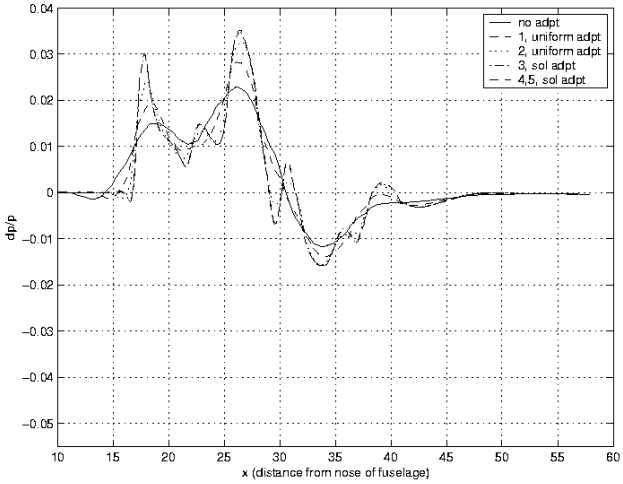

(a) Pressure distribution at r=9.5 in

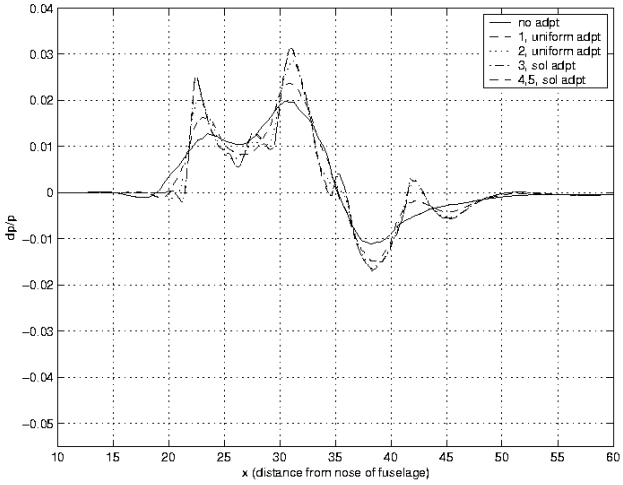

(b) Pressure distribution at r=12 in

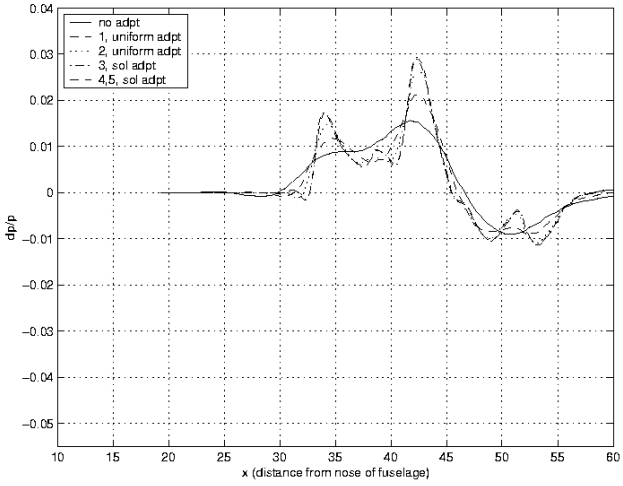

(c) Pressure distribution at r=18 in

Figure 16. Near-field pressure distributions for all adaptation cycles. Configuration without nacelles and tail.

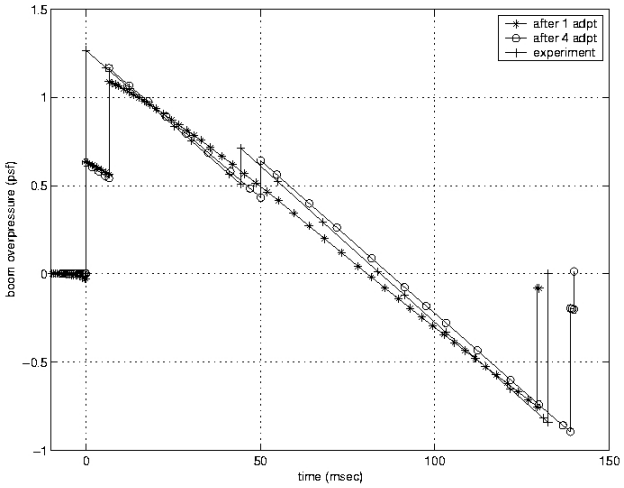

(a) Ground boom from r=9.5 in.

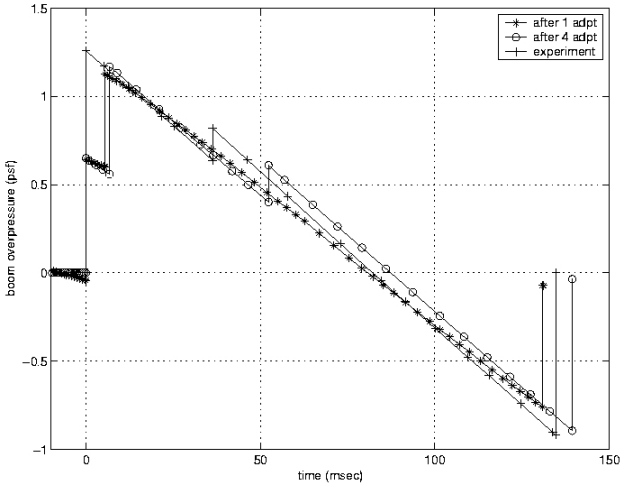

(b) Ground boom from r=12 in.

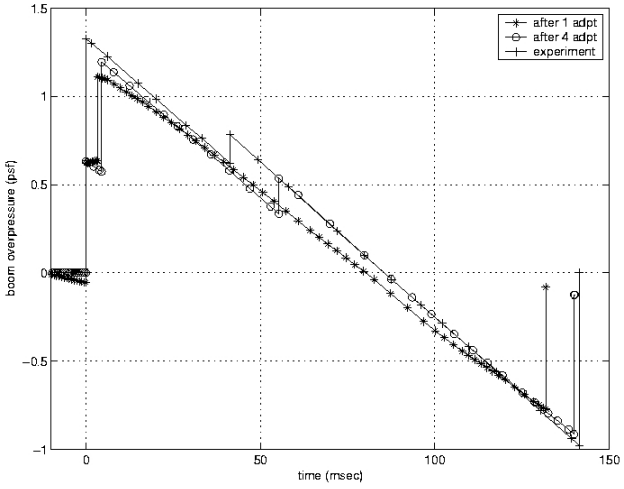

(c) Ground boom from r=18 in.

Figure 17. Ground boom comparisons. Complete configuration.

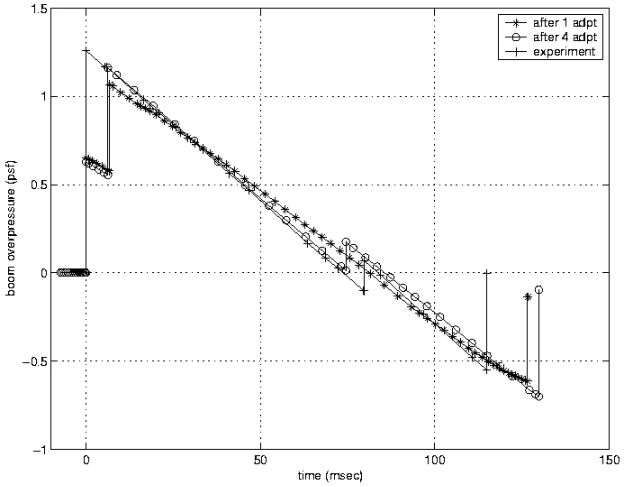

(a) Ground boom from r=9.5 in.

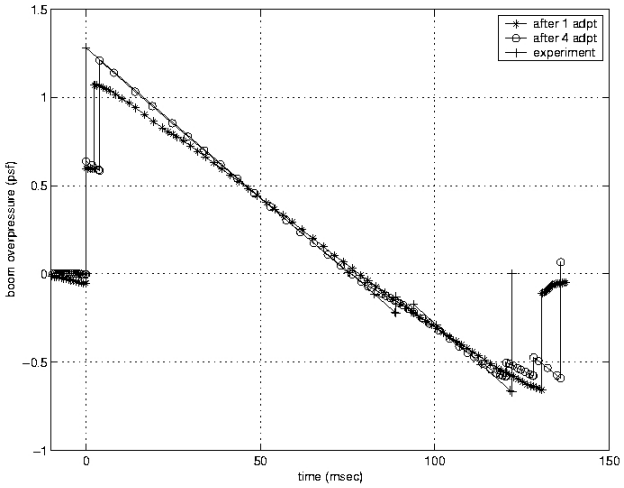

(b) Ground boom from r=18 in.

Figure 18. Ground boom comparisons. Configuration without nacelles.

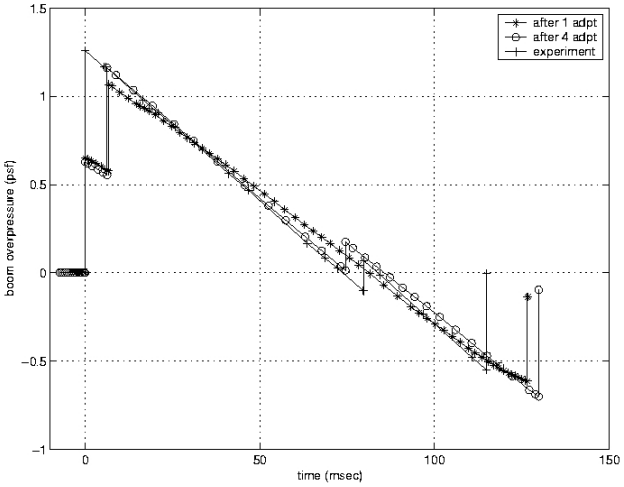

(a) Ground boom from r=9.5 in.

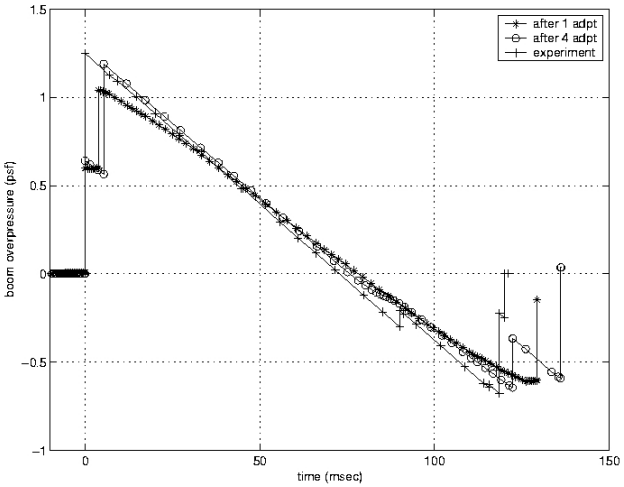

(b) Ground boom from r=18 in.

Figure 19. Ground boom comparisons. Configuration without nacelles and tail.

	Experiment		Computation		Deviation	
location	CSEL (dBC)	PL (PLdB)	CSEL (dBC)	PL (PLdB)	CSEL (dBC)	PL (PLdB)
r=9.5	101.60	95.70	99.61	91.76	1.99	3.94
r=12	101.80	96.15	99.84	92.53	1.96	3.62
r=18	102.25	95.46	100.22	90.68	2.03	4.78

Table 2. C-weighted sound exposure level (CSEL) and perceived loudness (PL) derived from experimental and computational data. (Complete configuration)

	Experiment		Computation		Deviation	
location	CSEL (dBC)	PL (PLdB)	CSEL (dBC)	PL (PLdB)	CSEL (dBC)	PL (PLdB)
r=9.5	100.27	93.38	97.86	88.26	2.41	5.12
r=18	100.78	91.87	98.46	85.14	2.32	6.73

Table 3. C-weighted sound exposure level (CSEL) and perceived loudness (PL) derived from experimental and computational data. (Configuration without nacelles)

	Experiment		Computation		Deviation	
location	CSEL (dBC)	PL (PLdB)	CSEL (dBC)	PL (PLdB)	CSEL (dBC)	PL (PLdB)
r=9.5	99.96	93.55	98.7	93.30	1.26	0.25
r=18	100.57	93.58	93.36	88.81	2.21	4.77

Table 4. C-weighted sound exposure level (CSEL) and perceived loudness (PL) derived from experimental data. (Configuration without nacelles and tail)